Journal of Marine Science and Technology

Volume 31 | Issue 1 Article 3

Deep learning–based, OceanTDLx sea ice detection model for SAR image

LIU Lin
Shandong University of Science and Technology, Qingdao, China.

LI Wanwu
Shandong University of Science and Technology, Qingdao, China., liwanwuqd@126.com

LI Hang
Shandong University of Science and Technology, Qingdao, China.

SUN Yi
Shandong University of Science and Technology, Qingdao, China.

Follow this and additional works at: https://jmstt.ntou.edu.tw/journal

 Part of the Fresh Water Studies Commons, Marine Biology Commons, Ocean Engineering Commons, Oceanography Commons, and the Other Oceanography and Atmospheric Sciences and Meteorology Commons

Recommended Citation

Lin, LIU; Wanwu, LI; Hang, LI; and Yi, SUN (2023) "Deep learning–based, OceanTDLx sea ice detection model for SAR image," *Journal of Marine Science and Technology*: Vol. 31: Iss. 1, Article 3.
DOI: 10.51400/2709-6998.2682
Available at: https://jmstt.ntou.edu.tw/journal/vol31/iss1/3

This Research Article is brought to you for free and open access by Journal of Marine Science and Technology. It has been accepted for inclusion in Journal of Marine Science and Technology by an authorized editor of Journal of Marine Science and Technology.

Deep learning–based, OceanTDLx sea ice detection model for SAR image

Acknowledgements

This research was supported by data from European Space Agency (ESA) and the Institute of Remote Sensing and Digital Earth, Chinese Academy of Sciences. Thank ESA and TensorFlow team for their software support.

This research article is available in Journal of Marine Science and Technology: https://jmstt.ntou.edu.tw/journal/vol31/iss1/3

RESEARCH ARTICLE

Deep Learning–Based, OceanTDLx Sea Ice Detection Model for SAR Image

Liu Lin, Li Wanwu*, Li Hang, Sun Yi

Shandong University of Science and Technology, Qingdao, China

Abstract

This study constructs four deep-learning OceanTDLx series models and uses a WinR-AdaGrad gradient descent algorithm to train and optimize the constructed models. Through an analysis of the loss, accuracy, and time consumption of the four models (i.e., OceanTDL2, OceanTDL3, OceanTDL5 and OceanTDL8), we reveal that the models' performance does not improve when the number of layers is increased and that OceanTDL5 provides the optimal performance. OceanTDL5 is compared with OceanTDA9 (a model that we previously constructed), and the curves for training loss_batch and training accuracy_batch indicate that OceanTDL5 is more suitable than OceanTDA9 for detecting distributed targets, particularly semi-melted sea ice, which is intertwined and easily confused with seawater. We process the SAR (Synthetic Aperture Radar) data of the research area and obtain a data set with a 10-m resolution, which is then used to verify the effectiveness of the constructed models for sea ice detection. The results reveal that OceanTDL5 has a detection capacity of approximately 55.6 km^2/s and a detection accuracy rate of 97.5%. Compared with traditional ocean target detection methods, OceanTDL5 has greater detection speed and accuracy.

Keywords: Polarimetric synthetic-aperture-radar data, Sea ice detection, Model construction, Deep learning, Neural network

1. Introduction

Ocean monitoring is the basis for developing, utilizing, and managing the ocean, which are activities that influence the long-term economic development and sovereignty of a country [1]. A key aspect of ocean monitoring is ocean target detection [2,3], which is becoming increasingly crucial for various civil and military applications. Ocean target detection is widely performed in the fields of disaster prevention and control, maritime search and rescue, fishery monitoring, ocean archaeology, customs anti-smuggling operations, environmental pollution monitoring, ocean security, and military operations [4,5]. Ocean targets can be divided into distributed targets and hard targets. A distributed target is a target that is distributed across a continuous and uninterrupted area of an ocean. The sea ice detection is a crucial aspect of the detection of distributed ocean targets, which is of great significance to maritime shipping.

The rapid development of artificial intelligence (AI) and machine learning (ML) have elevated target detection to a new stage of development. In contrast to traditional target detection methods that require the characteristics to be manually set, new target detection methods can extract characteristics automatically. To date, three main types of neural networks have been developed for ocean target detection.

(1) The first is target detection based on back propagation (BP) neural networks. Zakhvatkina et al. [6] classified the central-Arctic sea ice in

Received 1 July 2022; revised 2 December 2022; accepted 29 December 2022.
Available online 31 March 2023

* Corresponding author.
E-mail address: liwanwuqd@126.com (L. Wanwu).

https://doi.org/10.51400/2709-6998.2682
2709-6998/© 2023 National Taiwan Ocean University.

synthetic-aperture-radar (SAR) images by applying a BP neural network and a Bayesian algorithm, and their experimental results indicate that this method has a high classification accuracy. Sornam [7] used a BP neural network and an Otsu segmentation algorithm to detect SAR oil spills and demonstrated that this method provided greater accuracy relative to traditional statistical methods. Wibawa et al. [8] combined a BP neural network with a global image threshold method to detect ships in digital images, and they achieved an accuracy rate of 85%. Zakhvatkina et al. [9] combined a BP neural network with a supervised classification algorithm to detect sea ice, and their results reveal that the algorithm achieved a more favorable classification performance relative to other methods. Liu et al. [10] applied a BP neural network and contourlet transform theory to detect small infrared aerial targets, and their results indicate that their method was superior to several conventional algorithms in suppressing complex backgrounds. Jiang et al. [11] proposed a target detection algorithm for BP neural networks that is based on histogram statistics. Compared with traditional target detection algorithms, their algorithm is less complex while also being more efficient and accurate. Zhang et al. [12] used a classification method that is based on a BP neural network to detect sea ice in SAR images of Liaodong Bay, and their results revealed the favorable detection performance of their method.

(2) Target detection based on radial basis function (RBF) neural networks. Zhang et al. [13] proposed a new algorithm that is based on an RBF neural network and developed for background estimation and infrared small target detection. Their results indicate that their algorithm had a lower detection signal-to-noise ratio, greater stability, and greater operability relative to general infrared small target detection methods. Chen and Luo [14] constructed an RBF neural network predictor that is based on the theory of sea clutter chaos and developed to detect targets. Their experimental results reveal that their method was effective in detecting targets in a background with sea clutter. Li et al. [15] proposed an improved particle swarm optimization algorithm that is based on adaptive time-varying weights and local search operators; they applied it to the optimization learning of the parameters of an RBF neural network kernel function and verified it by using target ocean clutter data collected from the Dartmouth area. Li et al. [16] proposed an ocean clutter suppression method for ocean target imaging that is based on a chaotic neural network, and they extracted model parameters through an RBF neural network for target detection. Bojan and Davor [17] developed an RBF network coherent detection method for detecting targets in an ocean clutter with unknown statistical characteristics; they used simulated clutter samples and real sea clutter data to test the performance of the detection method, and their experimental results reveal that their method achieved a more favorable detection performance relative to other methods.

(3) Target detection based on convolutional neural networks (CNNs). Scholars have applied CNNs to perform ocean target detection. Chen et al. [18,19] proposed a CNN-based deep learning (DL) framework that is combined with a high spectrum and spatial resolution for target detection, and they demonstrated the high classification accuracy of the framework. Zhang et al. [20] constructed a scene classification framework for a gradient-boosted random convolution network; this framework can effectively combine multiple deep neural networks for target detection. Sharifzadeh et al. [21] proposed a neural network that is based on a hybrid algorithm comprising a CNN and a multilayer perceptron, and their results indicate that their algorithm provided a more favorable target classification performance relative to existing algorithms. Frederik et al. [22] used Faster R−CNN to detect and classify ocean targets, and they verified the effectiveness of their CNN for detecting ocean targets. Hu et al. [23] proposed a classification algorithm for a deep CNN and demonstrated the high classification accuracy of their proposed classification algorithm model for tidal flats. Du et al. [24] proposed a CNN-based hyperspectral target detection framework where a CNN is used to extract advanced characteristics for target detection; their experimental results reveal that their method was more accurate and robust that other conventional hyperspectral target detection algorithms. Wang et al. [25] proposed a hierarchical CNN−based method for detecting ship targets in spaceborne SAR images; their results indicate that their method achieved a more favorable performance relative to traditional constant false alarm rate (CFAR) technologies and CNN-based model. Cheng et al. [26] proposed a target detection algorithm that is based on an object-and-scene-context constrained CNN, and their experimental results

reveal the greater robustness and effectiveness of their method relative to other methods.

Sea ice can be detected through the extraction and classification of features from images. Jin et al. [27] used an unsupervised learning neural network and a self-organizing map (SOM; obtained from the output of an Earth Simulator ocean general circulation model) to extract the variability of the Kuroshio and Ryukyu currents in the East China Sea near the Kerama Gap. Their findings provide new insight into the exchange of water between the East China Sea and the Northwest Pacific. Liu et al. [28,29] used a SOM to analyze the sea surface height variability in the eastern region of the Gulf of Mexico; they then extracted spatial patterns of its circulation and identified the variations in sea level across various areas. Malmgren-Hansen et al. [30] proposed a CNN architecture, used ice density as a target probability for classification, and applied the architecture to predict Arctic sea ice; in their independent test set, they achieved a standard error of 0.89. Song et al. [31,32] proposed a sea ice classification method for SAR images that is based on residual CNNs and a long short-term memory (LSTM) network where spatial and temporal features are learnt; the method achieved favorable sea ice classification results when it was applied to a constructed data set.

Scholars have constructed DL models for ocean target detection on the basis of various neural networks. However, most studies have developed target detection models for ship target detection. Thus, the DL models for ship target detection are mature, whereas the models for distributed target detection (e.g., sea ice detection) require further development; moreover, few studies have verified the existing DL models for ocean target detection through large-scale experiments. In addition, because SAR data are unaffected by severe weather phenomena such as cirrus clouds and cloudy skies (they exhibit the all-weather characteristic), they provide several advantages for ocean target detection. Therefore, a DL-based sea ice detection model for SAR data is of practical value.

To solve the aforementioned problems, the present study uses SAR data to construct a lightweight DL model for sea ice target detection. The characteristics of the proposed model are as follows. First, the model can detect distributed targets such as sea ice; second, it is suitable for the characteristics of SAR data; third, it has been experimentally verified. In the first author's doctoral dissertation [33], the backscattering characteristics of ocean targets in SAR images (e.g., sea ice, seawater, and drilling platforms) were compared and analyzed; the results reveal 1) the mixing of seawater and sea ice in analyses of the ocean target backscattering histograms of SAR images and 2) the difficulty of detecting sea ice solely through threshold segmentation. To solve the aforementioned problems, the present study constructs several DL OceanTDLx series models for sea ice target detection. We preprocess the SAR image data obtained from the study area and use a self-designed program to generate a data set for sea ice detection that is suitable for DL. In a TensorFlow environment, four lightweight DL OceanTDLx series models are constructed for sea ice detection, and the training accuracy of the four models are compared and analyzed.

The remainder of the paper is organized as follows. Section 2.1 describes the processing (e.g., cropping, radiation correction, filtering, orthorectification, data format conversion) of the SAR data of the study area, which is performed to generate a data set for sea ice detection that is suitable for a DL model. Section 2.2 describes the construction of OceanTDLx series models that are suitable for SAR data and compatible with DL. Section 2.3 describes the proposed WinR-AdaGrad gradient descent training algorithm for optimizing the OceanTDLx series models; it also discusses the training loss_batch and training accuracy_batch curves of the models. Section 2.4 presents the results of a comparison between OceanTDL5 (constructed in the present study) and OceanTDA9 (constructed in a previous study) models with respect to training accuracy, loss, time consumption, and model size. Section 3 describes how the constructed model is used to verify the sea ice extraction in the study area and discusses the detection performance of the model. Section 4 summarizes the research results and discusses several avenues for future research.

2. Data and model

This section comprises four subsections. Section 2.1 introduces the research area and research data selected for the present study, the process through which the research data were processed, and the results obtained from the data. Section 2.2 describes the construction of the models, including the principle underlying the model's construction and the structure of the models. Section 2.3 describes the training process and the evaluation of model accuracy. Section 2.4 discusses the results of a comparison between the proposed distributed target detection model and a previously constructed detection model when applied to hard target detection.

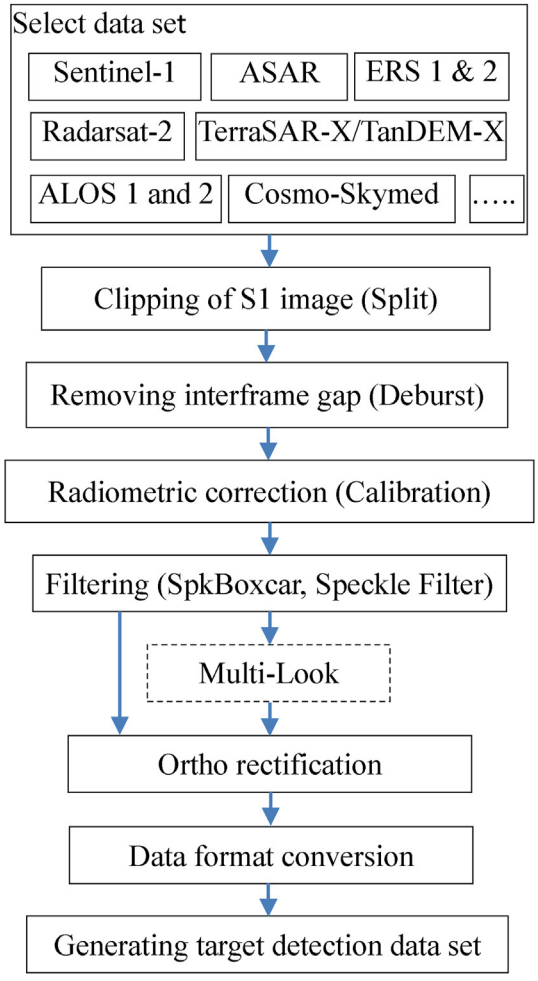

Fig. 1. Preprocessing flow of polarimetric synthetic-aperture-radar data.

2.1. Data

For a DL-based ocean target detection experiment, the Bohai Sea, which is located between 37°07′–40°56′ N and 117°33′–122°08′ E, is selected as the study area. The experimental data comprise the dual-polarimetric SAR data of Sentinel-1 (https://sentinel.esa.int/web/sentinel/missions) in the interferometric wide (IW) swath mode. Sentinel-1 comprises two satellites that share the same orbital plane and have a phase difference of 180°. These satellites can continuously provide radar maps of Earth, thereby ensuring the high revisit frequency, coverage, timeliness, and reliability of its results for applications where long-term series models are applied. A Sentinel-1 satellite can draw a global map every 12 days, the dual-satellite constellation provides an accurate repeating period of 6 days, and the repeating period at the North Pole is less than 1 day. The two Sentinel-1 satellites each carry a C-band SAR device with a center frequency of 5.405 GHz and support dual polarization (HH + HV, VV + VH) operations. Sentinel-1 SAR imaging can be performed in four modes, namely the stripmap (SM), IW, extra wide swath, and wave (WV) modes. The IW mode has a swath width of 250 km and a resolution of 5 × 20 m^2, and it is used to monitor sea ice areas and marine environments. Regardless of the weather conditions, it can cover a study area within 1–3 days. Because the accurate detection of parameters (e.g., sea ice contour) is necessary, the present study uses 20 IW-mode dual-polarimetric SAR scenes of the Bohai Sea, which were obtained between January and March 2016 when the area of sea ice in the Bohai Sea was the largest in recent years and accounted for almost 40% of the Bohai Sea area. The size of the data used is approximately 150 GB, and image data with a 10-m resolution are obtained after preprocessing. Preprocessing mainly involves image clipping, radiometric correction, filtering, ortho-rectification, and data format conversion. The preprocessing flow is presented in Fig. 1.

The speckle in SAR images degrades image quality and increases the difficulty of characteristic interpretation; thus, speckle filtering is a key step. The present study uses two polarization filters for

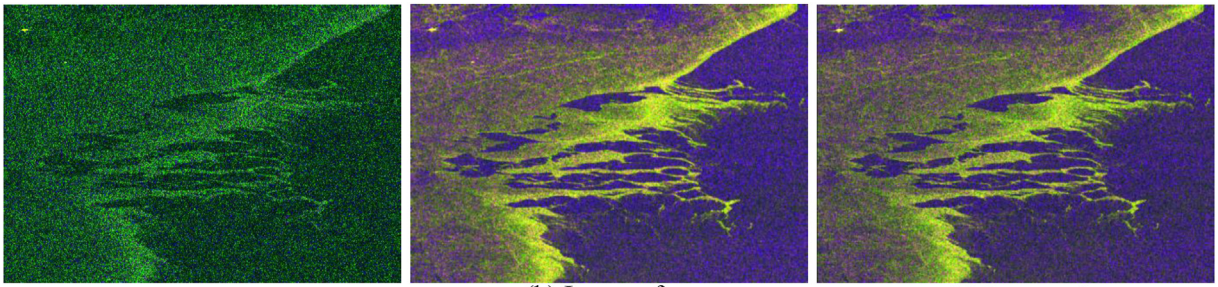

Fig. 2. Unfiltered image and color-coded images after polarimetric boxcar and improved Lee polarimetric filtering. Color coding for (a): R = Intensity_VH, G = Intensity_VV, B = Intensity_VH/Intensity_VV. *Color coding for (b) and (c):* R = C_{11}, G = C_{22}, B = C_{11}/C_{22}.

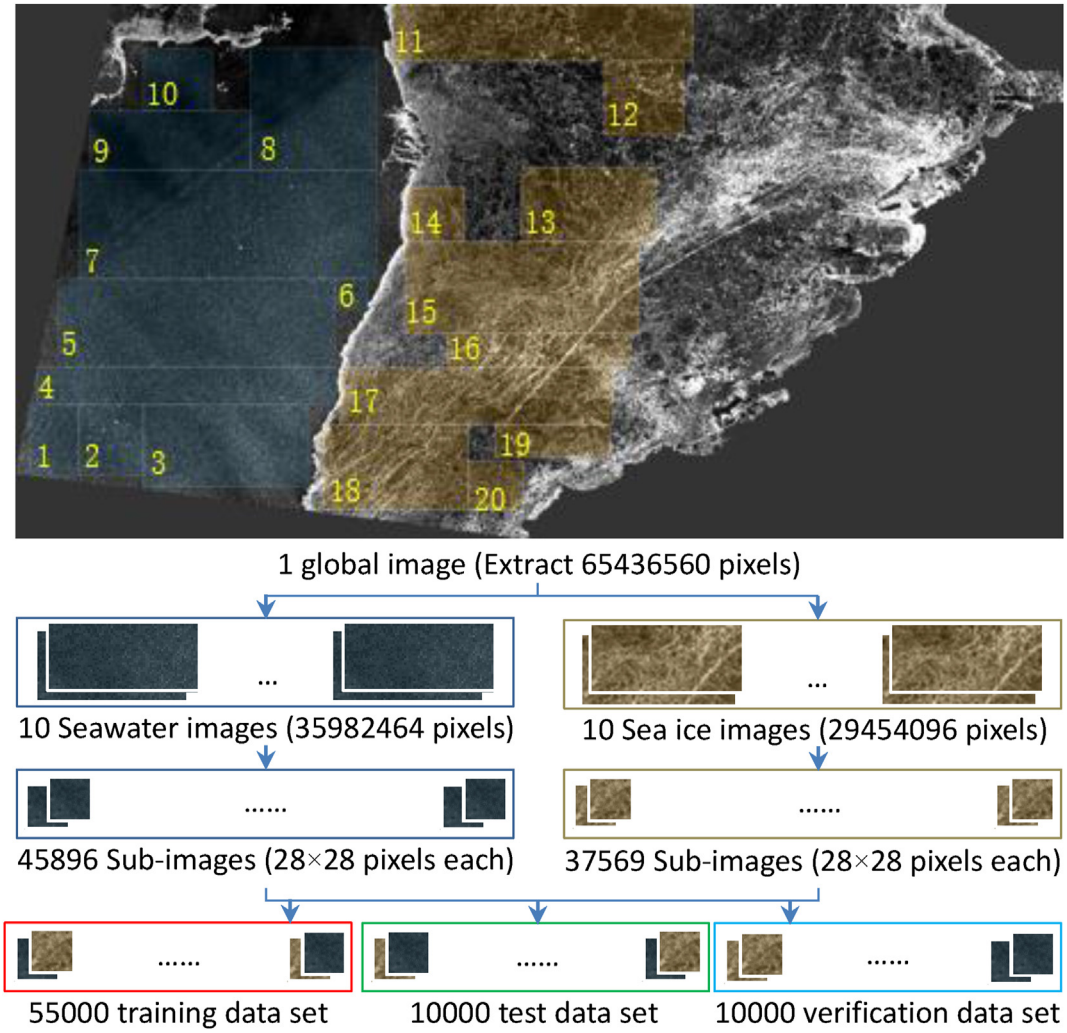

Fig. 3. Polarimetric synthetic-aperture-radar data set with 10-m resolution for ocean target detection.

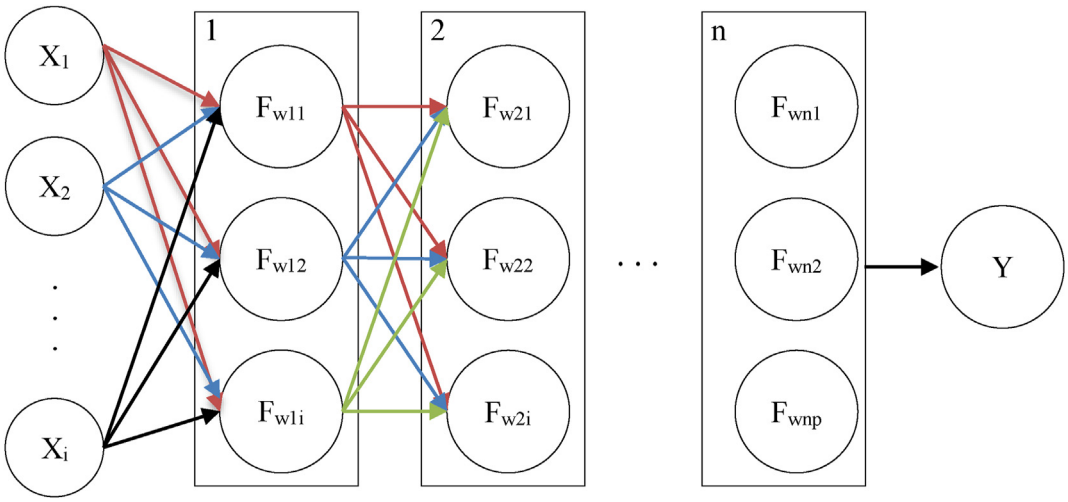

Fig. 4. Principle of deep-learning neural network.

filtering. The estimated covariance matrix of a polarimetric boxcar filter is given by formula (1) as follows [34]:

$$[\tilde{C}]_{i,j} = \langle [C]_{i,j} \rangle_{N_w} = \frac{1}{N_w^2} \sum_{p=-N_w/2}^{N_w/2} \sum_{q=-N_w/2}^{N_w/2} [C]_{i+p,j+q} \tag{1}$$

where i and j are the row and column of the corresponding pixel, respectively, and N_w is the size of the sliding window (i.e., the sliding window containing $N_w \times N_w$ pixels).

J. S. Lee polarimetric filter estimates an unspeckled covariance matrix by applying formula (2) as follows [35]:

$$[\tilde{C}] = \langle [C] \rangle + k([C] - \langle [C] \rangle) \tag{2}$$

where k is the proportionality coefficient as calculated using the span statistical value, namely $span = C_{11} + C_{22} + C_{33}$. Fig. 2 presents an unfiltered image and the color-coded versions of the image that are processed by polarimetric boxcar and improved Lee polarimetric filters for comparison; specifically, Fig. 2(a) presents the unfiltered image, Fig. 2(b) presents the image after polarimetric boxcar filtering, and Fig. 2(c) presents the image after improved Lee polarimetric filtering.

The improved Lee filter is used to filter and normalize an SAR image to [0, 255], and the obtained integer data image is resampled at a 10-m resolution. The final image contains a small number of drilling platforms and ships. The 65, 436, 560 pixel images are labeled, the label for sea ice targets is set to 1, and the label for seawater is set to 0; the data are saved as a polarimetric SAR data set for ocean target detection, which provide data sets for training, testing, and verification in the context of neural network learning (Fig. 3). In Fig. 3, the sections numbered 1−10 display seawater and comprise a total of 35 982 464 pixels (including 45 896 subimages with 28 × 28 pixels), the sections numbered 11−20 display sea ice and comprise a total of 29 454 096 pixels (including 37 569 subimages with 28 × 28 pixels).

The generated SAR data set, which has a 10-m resolution, is divided into three subdata sets, namely a training data set, test data set, and verification data set. The training data set contains 55 000 data pieces, and the test data set and verification data set contain 10 000 data pieces each.

2.2. Model construction

2.2.1. Principle of model

An ML neural network performs a weighted summation of the input data X and outputs the resulting data through an activation function. Its learning process involves identifying the most appropriate weighted method for maximizing the expectation of the output value Y, that is, minimizing the loss function. The operation of the network can be expressed as follows:

$$Y = F_W(X) = F(\langle X, W \rangle + b) \tag{3}$$

where W is the weight, b is the offset, $\langle X, W \rangle$ represents the inner product of the vectors X and W (i.e., the weighted summation or regression), and F is the activation function, which is generally a nonlinear function that serves as an adjustment made to achieve a given goal.

The DL neural network is presented in Fig. 4, where 1, 2 … n are hidden layers. When the output value is set as $Z_n(X)$, the output value of the first layer can be expressed as follows:

$$Z_1(X) = F[W_{11}X \quad W_{12}X \quad \ldots \quad W_{1i}X] \tag{4}$$

The output value of the nth layer is

$$Z_n(X) = F\left[W_{n1}Z_{n-1} \quad W_{n2}Z_{n-1} \quad \ldots \quad W_{np}Z_{n-1}\right] \tag{5}$$

After formula (4) is substituted into formula (5) and the offset is added, the output value Y after iteration can be obtained as follows:

$$Y = F\left(\begin{pmatrix} W_{11}X_1 + W_{12}X_2 + \ldots + W_{1i}X_m + b_1 \\ W_{21}X_1 + W_{22}X_2 + \ldots + W_{2j}X_m + b_2 \\ \ldots \\ W_{n1}X_1 + W_{n2}X_2 + \ldots + W_{np}X_m + b_n \end{pmatrix}\right) \tag{6}$$

During the training process, the activation function is adopted to perform nonlinear transformation, which is similar to kernel function decomposition. Neurons from multiple layers gradually extract data characteristics from multiple angles. The commonly used activation functions include sigmoid, tanh, and ReLu functions. Notably, an ReLu function is a nonsaturating activation function. When a value is excessively large or small, the derivative of sigmoid and tanh approaches zero but not for ReLu; thus, the use of a ReLu function can prevent a gradient from disappearing. In addition, an ReLu function can reduce overfitting and

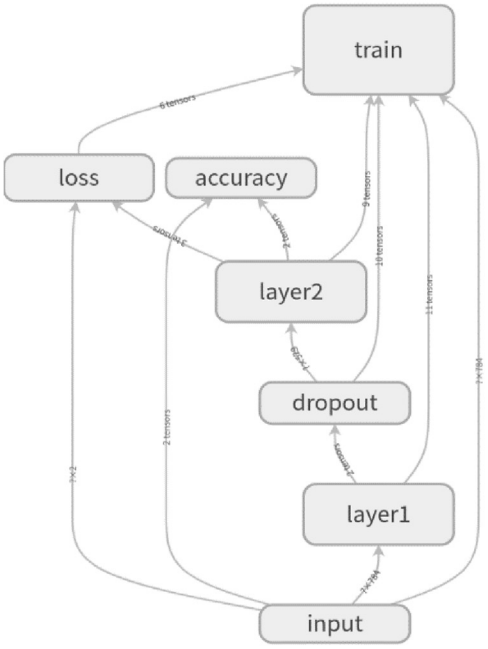

(a) OceanTDL2 model

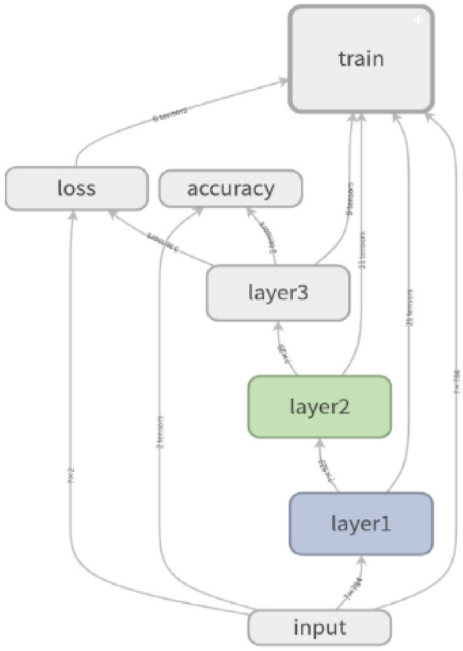

(b) OceanTDL3 model

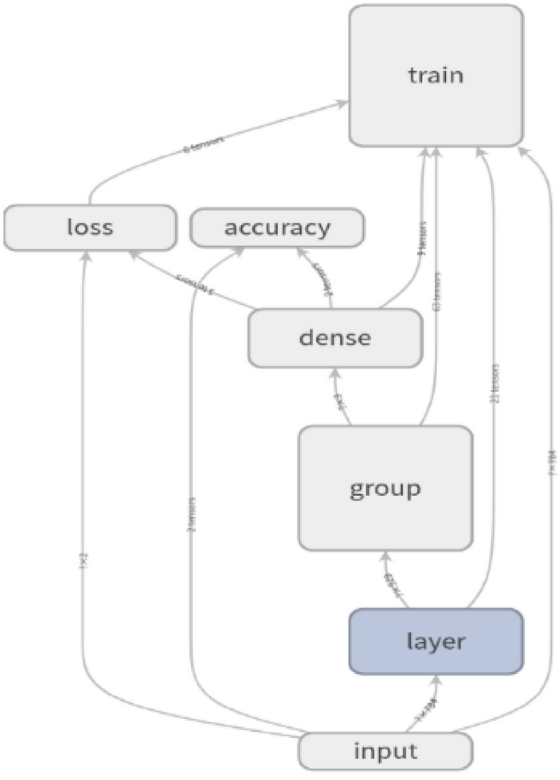

(c) OceanTDL5 model

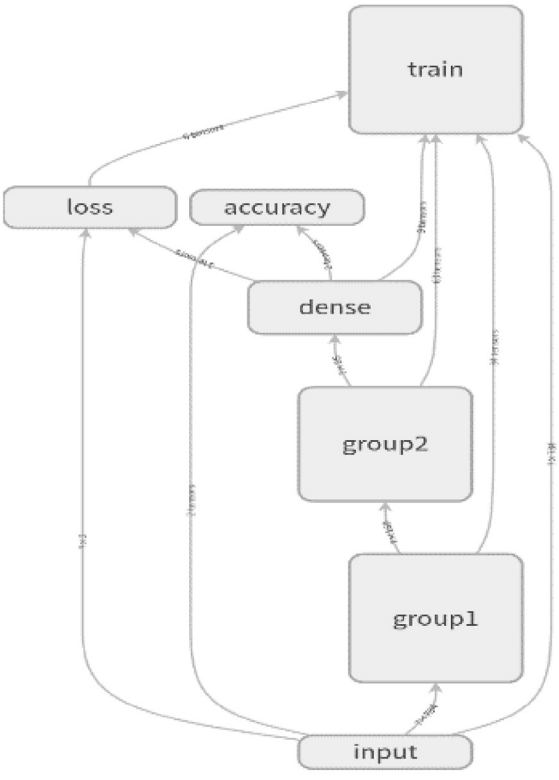

(d) OceanTDL8 model

Fig. 5. Four OceanTDLx models for sea ice detection.

enable faster network training because its derivative is easier to calculate relative to those of sigmoid and tanh functions. Therefore, an ReLu function is used in the present study.

2.2.2. *OceanTDLx modeling*

On the basis of the Mixed National Institute of Standards and Technology model [36], we expand the two-dimensional or three-dimensional images

to be detected into lines arranged as rows and construct several OceanTDLx series models for sea ice detection (i.e., L2, L3, L5, and L8 models). The model structures are presented in Fig. 5.

The structure of OceanTDL5 model comprises one layer, one Group and one fully connected Dense. The organization form of the layer is as follows: xW_pluse_b-relu-Dropout-reshape. The middle Group comprises three layers, and its organization form is as follows: (xW_pluse_b-relu-Dropout-reshape) × 3. The organizational form of the fully connected Dense is as follows: xW_pluse_b-relu. The amount of characteristic information is gradually reduced through the 529 → 121 → 25 → 9 process (from the 784 that is input at the beginning of the operation). Finally, the fully connected Dense, which contains nine neurons, is used to perform a weighted summation and ReLu activation to compress the number of characteristics to two, after which the two characteristics are input into a softmax loss function for classification.

The detailed parameters of the OceanTDLx models are listed in Table 1. In the table, (?, 784) in *x*-input column is defined as the inputting of a matrix with a size of a given row and 784 (28 × 28) columns. Accordingly, (784,529) in the weight row is a weight matrix with 784 rows and 529 columns. 2tensors in the output row is defined as the output of two tensors.

The structure of the OceanTDL5 model is detailed in Fig. 6. After several original images (28 × 28 pixels) containing sea ice and seawater are trained by OceanTDL5, we obtain model parameters that enable the model to distinguish between sea ice and seawater and save them in a model file for sea ice detection. The physical definitions of the parameters in Fig. 6 are identical to those presented in Table 1.

2.3. Accuracy analysis

We propose a WinR-AdaGrad gradient descent algorithm, where the loss function of parameter θ is set as $J(\theta)$ and the gradient for the parameter is the direction in which the function increases the fastest. The iterative update formulas are as follows:

$$\theta_t = \theta_{t-1} - \frac{\sqrt{\Delta\theta_{t-1}}}{\sqrt{\sum_{i=t_m}^{t} g_i^2 + \epsilon}} \odot g_t \tag{7}$$

$$\Delta\theta_t = \lambda \Delta\theta_{t-1} + (1-\lambda)\acute{g_t} \odot \acute{g_t} \tag{8}$$

where t is the current moment, t_m is the mth historical moment, and λ is the hyperparameter ($0 \leq \lambda < 1$) with a value that is generally 0.9. In formula (7), a small value ϵ is added to prevent the denominator from becoming 0. g_t is the minibatch stochastic gradient of the loss function$J(\theta)$ and expressed as:

$$g_t = \frac{\partial}{\partial\theta} J(\theta) = \sum_{j=t}^{t+x-1} \left(h_\theta\left(x_0^j, x_1^j, \ldots x_n^j,\right) - y_i \right) x_i^j \tag{9}$$

The proposed WinR-AdaGrad gradient descent training algorithm uses a window to limit the accumulation of gradient; that is, a subset is obtained by the window from the accumulated historical gradient for the learning rate to be adjusted.

This algorithm is used for model training. A model is mainly evaluated on the basis of training loss and accuracy; notably, training loss is based on the cross-entropy between the target classification and the model prediction classification. The formula applied is

$$J(\theta) = -\sum_{i=1}^{n} \left(y_{-i} \, log\left(h_\theta(x_i)\right) \right) \tag{10}$$

where y_{-i} is the value of the target classification input by the ith sample; $h_\theta(x_i)$ is the value of the model prediction classification of the ith sample x (i.e., y_i), n is the number of samples used for training, and $J(\theta)$ is the training loss.

The formula for calculating training accuracy is

$$accuracy = \frac{S_{True}}{S_{True} + S_{False}} \tag{11}$$

where S_{True} and S_{False}, respectively, refer to the number of samples correctly and incorrectly classified by a model in a single training iteration.

For OceanTDL8, the number of training iterations is set to 82 500; when the number of training iterations reaches 82 480 (i.e., within 300 iterations from concluding training), the exit condition for training is met, and the training is terminated. At this point, the loss is 0.0972, and the time taken is 4402 s. The average loss of the final 50 training iterations is 0.1416, and the standard deviation is 0.0158. Several experiments have demonstrated that when the OceanTDLx model is trained more than 40 000 times, a training accuracy of more than 97% is achieved, and the training loss reaches approximately 0.1. The loss_batch and accuracy_batch curves for model training approach an inflection point, and model performance exhibits no notable improvement with further training. For comparison, the OceanTDL5 model is set to have 82 500 training iterations, whereas the other two models are each set to have 41 250 training iterations. The effects of

Table 1. Parameters of OceanTDLx models.

OceanTDL2	Type	x-input	y-input	xW + b	Relu	Dropout	Reshape	xW + b	Relu			
	Input	(?,784)	(?,2)	(?,784)	(?,529)	2tensors	(?,529)	(?,529)	(?,2)			
	weights			(784,529)				(529,2)				
	bias			(529)				(2)				
	Output	(?,784)	(?,2), 2tensors	(?,529)	2tensors	(?,529)	(?,529)	(?,2)	3tensors, 2tensors			
OceanTDL3	Type	x-input	y-input	xW + b	Relu	Dropout	Reshape	xW + b	Relu	Dropout	Reshape	xW + b	Relu
	Input	(?,784)	(?,2)	(?,784)	(?,529)	2tensors	(?,529)	(?,529)	(?,25)	2tensors	(?,25)	(?,25)	(?,2)
	weights			(784,529)				(529,25)				(25,2)	
	bias			(529)				(25)				(2)	
	Output	(?,784)	(?,2), 2tensors	(?,529)	2tensors	(?,529)	(?,529)	(?,25)	2tensors	(?,25)	(?,25)	(?2)	3tensors, 2tensors
OceanTDL5	Type	x-input	y-input	xW + b	Relu	Dropout	Reshape	xW + b	Relu	Dropout	Reshape	xW + b	Relu
	Input	(?,784)	(?,2)	(?,784)	(?,529)	2tensors	(?,529)	(?,529)	(?,121)	2tensors	(?,121)	(?,9)	(?,2)
								(?,121)	(?,25)	2tensors	(?,25)		
								(?,25)	(?,9)	2tensors	(?,9)		
	weights			(784,529)				(529,121)				(9,2)	
								(121,25)					
								(25,9)					
	bias			(529)				(121)				(2)	
								(25)					
								(9)					
	Output	(?,784)	(?,2), 2tensors	(?,529)	2tensors	(?,529)	(?,529)	(?,121)	2tensors	(?,121)	(?,121)	(?,2)	3tensors, 2tensors
								(?,25)	2tensors	(?,25)	(?,25)		
								(?,9)	2tensors	(?,9)	(?,9)		
OceanTDL8	Type	x-input	y-input	xW + b	Relu	Dropout	Reshape	xW + b	Relu	Dropout	Reshape	xW + b	Relu
	Input	(?,784)	(?2)	(?,784)	(?,625)	2tensors	(?,625)	(?,169)	(?,81)	2tensors	(?,81)	(?,25)	(?,2)
				(?,625)	(?,441)	2tensors	(?,441)	(?,81)	(?,49)	2tensors	(?,49)		
				(?,441)	(?,289)	2tensors	(?,289)	(?,49)	(?,25)	2tensors	(?,25)		
				(?,289)	(?,169)	2tensors	(?,169)						
	weights			(784,625)				(169,81)				(25,2)	
				(625,441)				(81,49)					
				(441,289)				(49,25)					
				(289,169)									
	bias			(625)				(81)				(2)	
				(441)				(49)					
				(289)				(25)					
				(169)									
	Output	(?,784)	(?,2), 2tensors	(?,625)	2tensors	(?,625)	(?,625)	(?,81)	2tensors	(?,81)	(?,81)	(?,2)	3tensors, 2tensors
				(?,441)	2tensors	(?,441)	(?,441)	(?,49)	2tensors	(?,49)	(?,49)		
				(?,289)	2tensors	(?,289)	(?,289)	(?,25)	2tensors	(?,25)	(?,25)		
				(?,169)	2tensors	(?,169)	(?,169)						

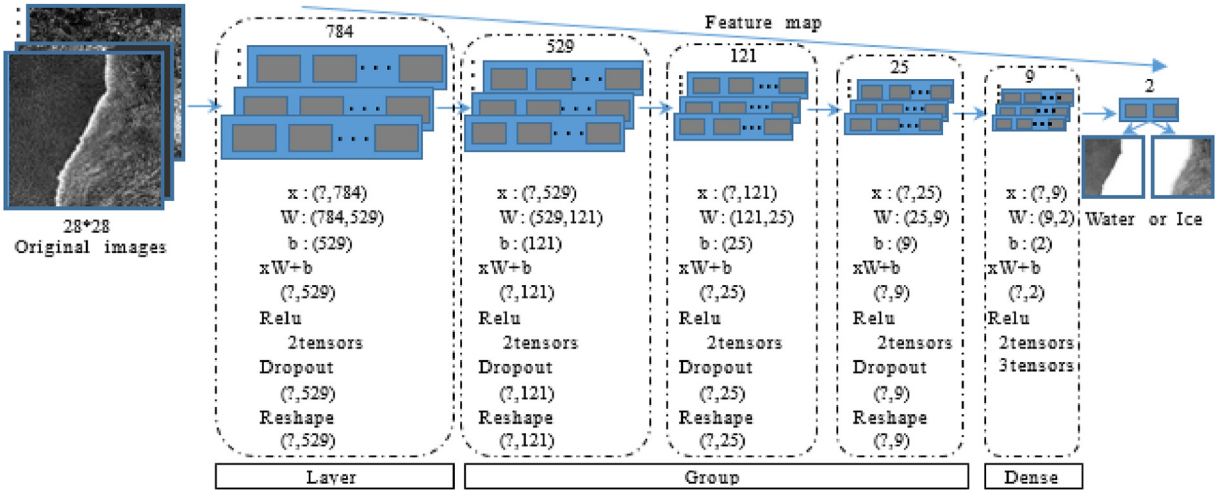

Fig. 6. Structure of OceanTDL5 (Group includes three convolutional layers, Dropout, and reshaping).

the models and parameters on training accuracy, training loss, time taken, and generated model size are summarized in Table 2. The loss fluctuation is large initially and then gradually decreases with training. The training loss_batch curves for the models are presented in Fig. 7(a), and the training accuracy_batch curves are presented in Fig. 7(b). OceanTDL2 exhibits the lowest loss decline rate, followed by OceanTDL8, OceanTDL3, and OceanTDL5. Within the first 20 000 training iterations, OceanTDL2 exhibits the largest fluctuation for loss decline, and OceanTDL5 exhibits the highest loss decline rate and highest level of fluctuation stability. Therefore, among the models, OceanTDL5 provides the highest training accuracy.

2.4. Comparative analysis

The OceanTDL5 model is compared with the ocean target detection model OceanTDA9, which was previously constructed by the authors [37,38]. The training loss_batch curves of the two models are presented in the left hand side of Fig. 8, which reveals that the loss of OceanTDL5 quickly decreases to less than 0.2 before stabilizing. After 60 000 training iterations, the results of OceanTDL5 and OceanTDA9 intersect, the loss of OceanTDL5 approaches 0.10, and almost 2476 s is taken (less than the time required for the loss of OceanTDA9 to approach 0.10). The training accuracy_batch curves of OceanTDL5 and OceanTDA9 are presented in the right hand side of Fig. 8. The accuracy of OceanTDL5 model quickly reaches 0.950 and increases slowly thereafter. After 60 000 training iterations, the accuracy of OceanTDL5 approaches 0.98, which requires almost 2476 s; thereafter, the accuracy of OceanTDL5 mostly stabilizes.

The effects of the model parameters of OceanTDL5 and OceanTDA9 on training accuracy, training loss, time taken, and the generated model size are presented in Table 3.

In summary, in the context of practical ocean target detection, the OceanTDL5 model is more suitable than the other models for distributed targets such as semi-formed or semi-melted sea ice that intermingle and are easily confused with seawater.

3. Results

We use the constructed OceanTDL2 and OceanTDL5 models to conduct sea ice detection experiments and compare the results. For OceanTDL2, the number of training iterations is set to 8250. When the model is trained 8090 times, that is, within 300 iterations of the conclusion of training,

Table 2. Effects of OceanTDLx models and parameters on training results.

Model	Number of layers	Training times	Accuracy		Loss		Time [s]	Model size [MB]
		Set/Actual	Test	Average	Test	Average		
OceanTDL2	2	41250/41230	0.9858	0.9707	0.0935	0.1311	1699	1.7
OceanTDL3	3	41250/41090	0.9791	0.9698	0.1023	0.1235	1684	1.7
OceanTDL5	5	82500/82470	0.9902	0.9811	0.0722	0.1008	3424	1.9
OceanTDL8	8	82500/82480	0.9845	0.9702	0.0972	0.1416	4402	3.9

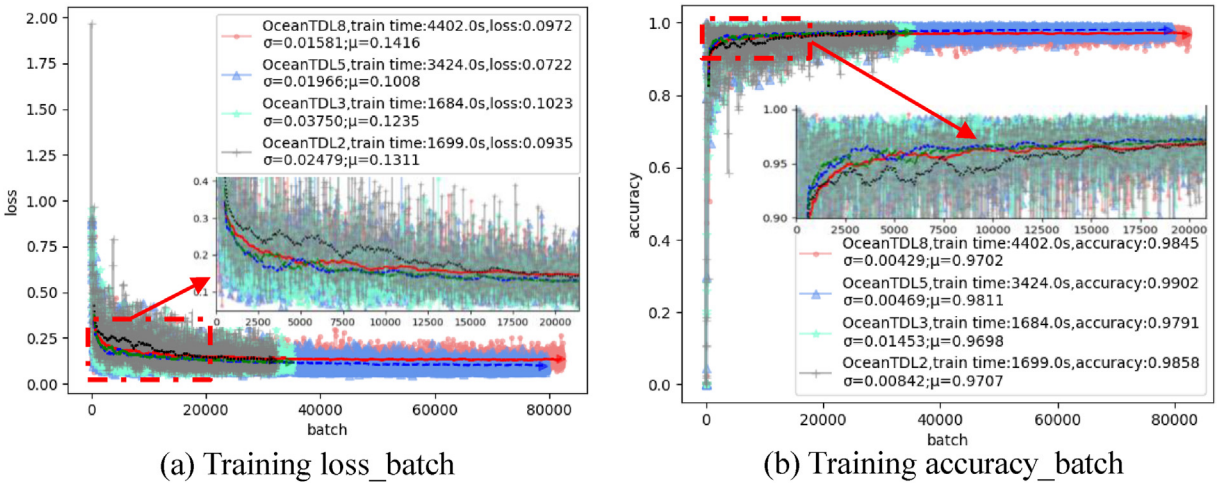

(a) Training loss_batch (b) Training accuracy_batch

Fig. 7. Training loss_batch and accuracy_batch of OceanTDLx model.

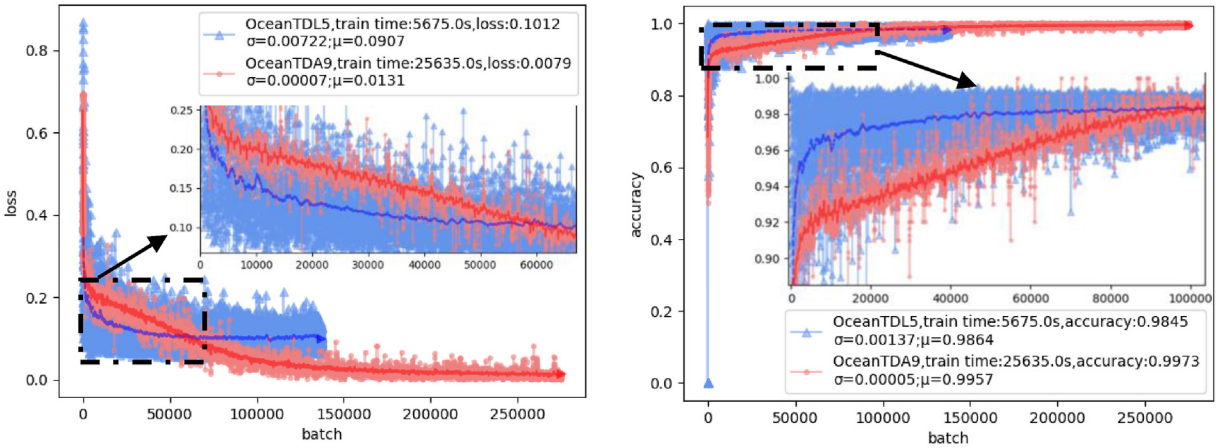

(a) Training loss_batch (b) Training accuracy _batch

Fig. 8. Training loss_batch and accuracy_batch of OceanTDL5 and OceanTDA9.

the exit condition for training is met, and the training is terminated. At this time, the loss is 0.1034, the accuracy is 0.9847, and the time taken is 158 s. The average model loss for the final 50 training iterations is 0.2650, and its standard deviation is 0.075. The average model accuracy is 0.8925, and its standard deviation is 0.0449. The training loss and accuracy curves for OceanTDL2 vary by batch (indicated by the blue dashed lines in Fig. 9); Fig. 9(a) presents the training loss_batch curve, and Fig. 9(b) presents the training accuracy_batch curve.

The number of training iterations for OceanTDL5 is set to 8250. After the model is trained 8170 times, that is, within 300 iterations of the conclusion of training, the exit condition for training is met, and training is terminated. At this time, the loss is 0.1801, the accuracy is 0.9597, and the time taken is 166 s. The average model loss for the final 50 training iterations is 0.2776, and its standard deviation is 0.0381. The average model accuracy is 0.8825, and its standard deviation is 0.0130. The training loss and accuracy curves for OceanTDL5 vary by batch

Table 3. Effects of model parameters of OceanTDL5 and OceanTDA9 on training results.

Model	Number of layers	Training times	Accuracy		Loss		Time [s]	Model size [MB]
		Set/Actual	Test	Average	Test	Average		
OceanTDL5	5	137500/137490	0.9845	0.9864	0.1020	0.0907	5675	1.9
OceanTDA9	9	500/275000	0.9973	0.9957	0.0079	0.0131	25635	15.9

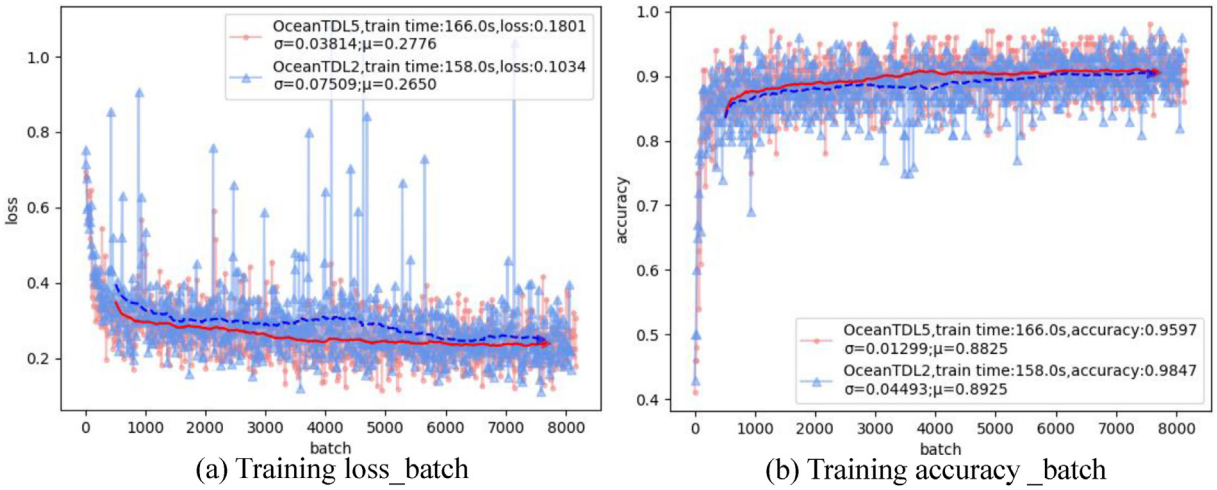

Fig. 9. Training loss_batch and accuracy_batch of OceanTDL2 and OceanTDL5.

Table 4. Training results for sea ice detection models.

Model	Number of layers	Training times	Accuracy		Loss		Time [s]	Model size [MB]
		Set/Actual	Test	Average	Test	Average		
OceanTDL2	2	8250/8090	0.9847	0.8925	0.1034	0.2650	158	1.7
OceanTDL5	5	8250/8170	0.9597	0.8825	0.1801	0.2776	166	1.9

(indicated by the red solid lines in Fig. 9). The results of the two models at the termination of training are presented in Table 4. Fig. 9 reveals that the smoothing of the training loss_batch and accuracy_batch curves of OceanTDL5 is more favorable than that of OceanTDL2 and that the overall training loss and training accuracy results of OceanTDL5 are more favorable than those of OceanTDL2.

The sea ice detected by the trained OceanTDL2 model is indicated in Fig. 10(a), where the detected sea ice are indicated by magenta boxes and the black sections indicate seawater. Fig. 10(a) contains

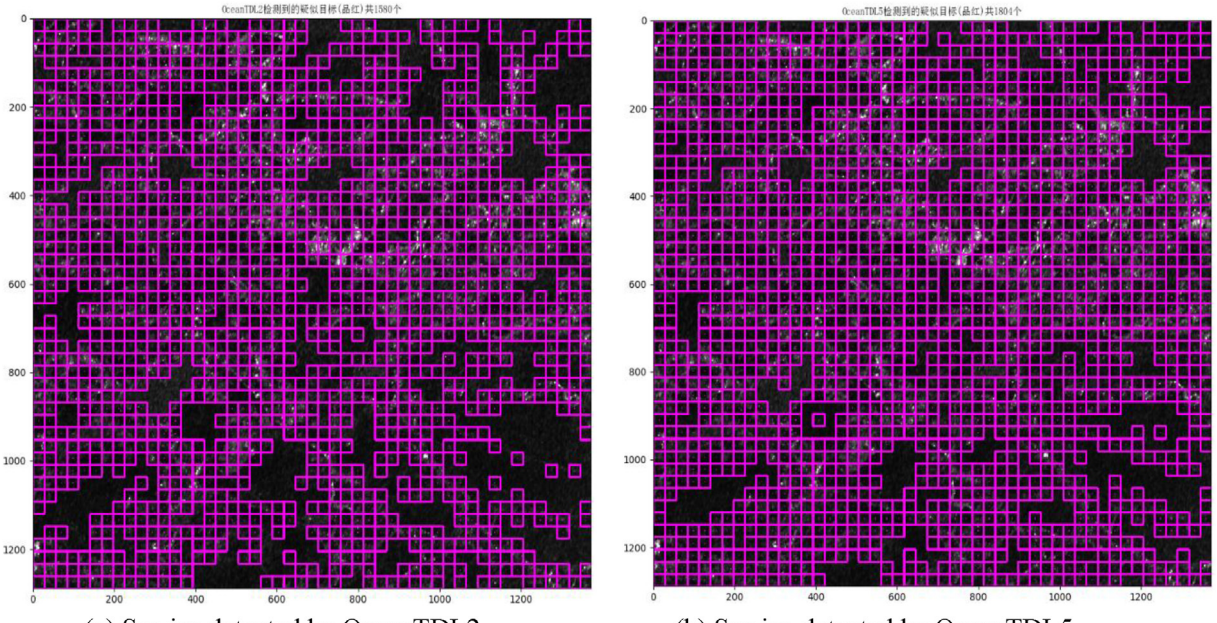

Fig. 10. Sea ice detected by OceanTDL2 and OceanTDL5; results indicate that OceanTDL5 is more accurate.

Table 5. Results for detection of sea ice.

Model name	Sample amounts	Sea ice amounts	Detection amounts	Missed detection amounts	Detection rate	Missed detection rate	Time [s]
OceanTDL2	2250	1849	1580	269	85.5%	14.5%	3.19
OceanTDL5	2250	1851	1804	47	97.5%	2.5%	3.17

1580 sea ice sections (28 × 28 pixels each) and 674 seawater sections. The missed detection rate for sea ice is 14.5%, the detection time is 3.19 s, and the detection capacity for SAR images with a 10-m resolution is almost 55.3 km^2/s.

The sea ice detected by the trained OceanTDL5 model is indicated in Fig. 10(b), which contains 1804 sea ice sections (28 × 28 pixels each) and 446 seawater sections. The detection rate for sea ice is 97.5%, the missed detection rate is 2.5%, the detection time is 3.17 s, and the detection capacity for SAR images with a 10-m resolution is almost 55.6 km^2/s.

The final sea ice detection results obtained through OceanTDL2 and OceanTDL5 are presented in Table 5. The sea ice detection rate for OceanTDL5 is 12% higher than that of OceanTDL2. For a given sample size, the detection speed of OceanTDL5 is slightly higher than that of OceanTDL2. The undetected sea ice is mainly concentrated in the sections where seawater and sea ice mix, that is, sections where semi-melted ice or water are found on ice.

4. Conclusion

Ocean target detection is a key technical aspect in fields such as marine disaster prevention and control, marine environmental protection, marine resource development, marine military monitoring, and marine sovereignty maintenance. The present study applies AI to sea ice detection and constructs DL-based sea ice detection models. The main contributions and conclusions of the present study are as follows.

(1) The present study constructs four lightweight OceanTDLx series models for sea ice detection, namely OceanTDL2, OceanTDL3, OceanTDL5, and OceanTDL8.
(2) A WinR-AdaGrad gradient descent algorithm for training the four models is proposed, and the training loss and accuracy of each model are analyzed. The results indicate that increasing the number of layers in a model does not increase the model's accuracy. OceanTDL5 is revealed to have the highest accuracy among the developed models.
(3) OceanTDLx is analyzed and compared with a CNN-based OceanTDAx model previously constructed by the authors. The results indicate that OceanTDLx is more suitable for detecting distributed targets such as sea ice, whereas OceanTDAx is more suitable for detecting hard targets such as drilling platforms.
(4) The polarimetric SAR data of the study area is preprocessed to obtain a data set with a 10-m resolution, and the data set is used with the constructed DL model to conduct sea ice detection experiments. The results reveal a detection capacity of almost 55.6 km^2/s and a detection accuracy rate of 97.5%. Compared with traditional ocean target detection methods, the constructed DL model provides greater detection speed and accuracy.

Given the present findings, the next step is to integrate an attention mechanism and a human visual nerve mechanism into the DL sea ice detection model for SAR imaging to further improve the models sea ice detection accuracy. The proposed model can be deployed through a multicore distributed computing device and operated in parallel to improve its operating efficiency and detection speed.

Data availability

The datasets used and analyzed during the current study are available from the corresponding author upon reasonable request.

Funding statement

This work was supported by the Natural Science Foundation of Shandong Province (NO.ZR2019MD034) and the Education Reform Project of Shandong Province (NO.M2020266).

Conflict of interest

The authors declare no conflict of interest.

Acknowledgments

This research was supported by data from European Space Agency (ESA) and the Institute of Remote Sensing and Digital Earth, Chinese Academy of Sciences. Thank ESA and TensorFlow team for their software support.

References

[1] Zhao Z. Research on the key technologies for ship surveillance by integration of space-borne SAR and AIS. National University of Defence Technology; 2013.

[2] Marino A. Notch filter for ship detection with polarimetric SAR data. IEEE J Sel Top Appl Earth Obs Rem Sens 2013;6(3): 1219−32.

[3] Gambardella A, Nunziata F, Migliaccio M. A physical full-resolution SAR ship detection filter. IEEE Transactions on Geoscience and Remote Sensing Letters 2008;5(4):760−3.

[4] Cui SP. Target detection in sea clutter based on time-frequency analysis. Harbin Institute of Technology; 2014.

[5] Tae-Ho Kim, Chan-Su Yang, Kazuo Ouchi. Interpretation of SAR image modulation by the interaction of current and bottom topography in gyeonggi Bay with microwave scattering models. J Mar Sci Technol 2016;24(6):15.

[6] Zakhvatkina NY, Alexandrov VY, Johannessen OM, Sandven S, Frolov IY. Classification of sea ice types in ENVISAT synthetic aperture radar images. IEEE Trans Geosci Rem Sens 2013;51(5): 2587−600.

[7] Sornam M. Oil spill and look-alike spots from SAR imagery using Otsu method and artificial neural network. International Journal of Engineering Technologies and Management Research 2017;4(11):1−10.

[8] Wibawa HA, Sasongko PS. Detection of ship using image processing and neural network. Telkomnika 2018;16(1):259−64.

[9] Zakhvatkina N, Smirnov V, Bychkova I. sea ice classification based on neural networks method using sentinel-1 data. In: International Multidisciplinary Scientific GeoConference: SGEM 2019;19(2.2):617−23.

[10] Liu G, Wang F, Liu ZH. Infrared aerial small target detection based on digital image processing. Multimed Tool Appl 2017; 76(19):19809−23.

[11] Jiang S, Pang YL, Wang LY, Yu JY, Cheng BW, Li ZL. A target detection algorithm of neural network based on histogram statistics. In: IGARSS 2020-2020 IEEE international geoscience and Remote sensing symposium. IEEE; 2020. p. 1628−31.

[12] Zhang X, Zhang J, Ji YG. Sea ice detection from SAR images of the Liaodong Bay based on texture analysis. Adv Mar Sci 2008;3:386−93.

[13] Zhang Y, Shen ZK, Wang P. Background estimation and the infrared small target detection based on RBF neural network. J Natl Univ Def Technol 2004;5:39−45.

[14] Chen Y, Luo PF. Target detection in sea clutter based on RBF neural network. Radar Science and Technology 2005;5:18−22.

[15] Li ZX, Yin ZD, Shi J. PSO-RBF small target detection in sea clutter background. Communications, Signal Processing, and Systems 2020:1044−51.

[16] Li ZZ, Chen J, Shen MR, Hou Q. sea clutter suppression approach for target images at sea based on chaotic neural network. J Optoelectron - Laser 2014;25(3):588−94.

[17] Bojan V, Davor B. Mitigation of the effects of unknown sea clutter statistics by using radial basis function network. Radiotehnika 2020;29:215−27.

[18] Chen YS, Lin ZH, Zhao X, Wang G. Deep learning-based classification of hyperspectral data. IEEE J Sel Top Appl Earth Obs Rem Sens 2014;7(6):2094−107.

[19] Chen YS, Zhao X, Jia XP. Spectral−spatial classification of hyperspectral data based on deep belief network. IEEE J Sel Top Appl Earth Obs Rem Sens 2015;8(6):1−12.

[20] Zhang F, Du B, Zhang LP. Scene classification via a gradient boosting random convolutional network framework. IEEE Trans Geosci Rem Sens 2015;54(3):1−10.

[21] Sharifzadeh F, Akbarizadeh SeifiKavian GY. Ship classification in SAR images using a new hybrid CNN−MLP classifier. Journal of the Indian Society of Remote Sensing 2018;47: 551−62.

[22] Frederik ETS, Martin PFI, Jonathan DS, Mogens B. Assessing deep-learning methods for object detection at sea from LWIR images. IFAC-PapersOnLine 2019;52(21):64−71.

[23] Hu YB, Zhang J, Ma Y, Li XM. Deep learning classification of coastal wetland hyperspectral image combined spectra and texture features: a case study of huanghe (yellow) river estuary wetland. Acta Oceanol Sin 2019;38(5):142−50.

[24] Du JM, Li ZY, Sun H. CNN-based target detection in hyperspectral imagery. In: IGARSS 2018-2018 IEEE international geoscience and Remote sensing symposium. IEEE; 2018. p. 2761−4.

[25] Wang J, Zheng T, Lei P, Bai X. A hierarchical convolution neural network (CNN)-Based ship target detection method in spaceborne SAR imagery. Rem Sens 2019;11(6):620.

[26] Cheng B, Li ZZ, Xu BT, Dang CJ. Target detection in Remote sensing image based on object-and-scene context constrained CNN. Geosci Rem Sens Lett IEEE 2021;19:1−5.

[27] Jin B, Wang G, Liu Y, Zhang R. Interaction between the East China sea Kuroshio and the Ryukyu current as revealed by the self-organizing map. J Geophys Res: Oceans 2010; 115(C12).

[28] Liu Y, Weisberg RH, Vignudelli S, Mitchum GT. Patterns of the loop current system and regions of sea surface height variability in the eastern Gulf of Mexico revealed by the self-organizing maps. J Geophys Res: Oceans 2016;121(4): 2347−66.

[29] Liu Y, Weisberg RH, He R. Sea surface temperature patterns on the West Florida Shelf using growing hierarchical self-organizing maps. J Atmos Ocean Technol 2006;23(2): 325−38.

[30] Malmgren-Hansen D, Pedersen LT, Nielsen AA, Kreiner MB, Saldo R, Skriver H, et al. A convolutional neural network architecture for Sentinel-1 and AMSR2 data fusion. IEEE Trans Geosci Rem Sens 2020;59(3):1890−902.

[31] Song W, Li MH, Gao W, Huang DM, Ma ZL, Liotta A, et al. Automatic sea-ice classification of SAR images based on spatial and temporal features learning. IEEE Trans Geosci Rem Sens 2021;59(12):9887−901.

[32] Song W, Gao W, He Q, Liotta A, Guo WQ. SI-STSAR-7: a large SAR images dataset with spatial and temporal information for classification of winter sea ice in hudson Bay. Rem Sens 2021;14(1):168.

[33] Wanwu L. Marine target detection for SAR image based on deep learning. Shandong University of Science and Technology; 2021.

[34] Lee JS, Pottier E. Polarimetric radar imaging: from basics to applications. CRC Press; 2017.

[35] Vasile G, Trouve E, Lee JS, Buzuloiu V. Intensity-driven adaptive-neighbourhood technique for polarimetric and interferometric SAR parameters estimation. IEEE Trans Geosci Rem Sens 2006;44(6):1609−21.

[36] Li D. The MNIST database of handwritten digit images for machine learning research [best of the web]. IEEE Signal Process Mag 2012;29(6):141−2.

[37] Wanwu L, Lin L*, Jixian Z. Fusion of SAR and optical image for sea ice extraction. J Ocean Univ China 2021;20(6): 1440−50.

[38] Wanwu L, Lin L*, Jixian Z. AdaRW training optimization algorithm for deep learning model of marine target detection based on SAR. Int J Rem Sens 2022;43(1):120−31.